Earth and Planetary Science Letters 618 (2023) 118271

Contents lists available at ScienceDirect

Earth and Planetary Science Letters

journal homepage: www.elsevier.com/locate/epsl

2000 yrs of earthquakes inferred from subsidence events on the Imperial fault, California: Effect of lake-level changes and implication for variable slip rates

Thomas K. Rockwell [a,*], Yann Klinger [b]

[a] Dept. Geological Sciences, San Diego State University, San Diego, CA 92182, United States of America
[b] Université de Paris Cité, Institut de physique du globe de Paris, CNRS, Paris, France

ARTICLE INFO

Article history:
Received 17 November 2022
Received in revised form 30 May 2023
Accepted 9 June 2023
Available online 29 June 2023
Editor: R. Bendick

Keywords:
Imperial fault
cone penetrometer paleoseismology
lake loading and earthquake triggering

ABSTRACT

The Salton Trough has filled repeatedly with freshwater Lake Cahuilla from avulsions of the Colorado River. The relationship between lake fillings and large earthquakes is a topic of debate. From a new study on the Imperial fault applying cone penetrometer soundings, we show that the long hiatus in lake fillings between about ca 100 BCE and 950 CE resulted in accelerated slip in the few hundred years after re-inundation, an observation that is also seen on the San Andreas and southern San Jacinto faults. A regional, basin-wide signal of transient accelerated slip is interpreted to be the result of the effects of increased pore pressure on fault strength resulting from the 100 m of water load during full lake inundations. These results demonstrate the effects of dramatically increasing pore pressure, termed the reservoir induced seismicity effect, on fault activity and explain the current "earthquake drought" on the southernmost section of the San Andreas fault.

1. Introduction

Understanding the timing of earthquakes along fault systems remains a major endeavor in Earth sciences. Long time series of earthquakes built on paleoseismological data show that the time distribution of earthquakes along a fault system can vary through time with periods of intense seismic activity separated by periods of long seismic quiescence (Stein et al., 1997; Scharer and Streig, 2019; Lefevre et al., 2018). Earthquake-triggering mechanisms have been proposed (King et al., 1994; Freed et al., 2007) to explain such variability, which to date are not reaching any consensus. A direct consequence of such short-term changes in seismicity rate is that the local slip-rate also has to vary, although it averages out over longer time periods (Wechsler et al., 2018). Unexpectedly, induced seismicity related to human activity sheds new light on such processes by allowing unambiguous correlation between changes in fluid pore pressure in the ground and seismicity (Healy et al., 1968; Raleigh et al., 1976; Ellsworth, 2013; Keranen et al., 2014; Keranen and Weingarten, 2018), and although more tenuous, seasonality of seismicity (Bettinelli et al., 2008) in monsoon prone areas is pointing toward the existence of a similar process for natural microseismicity. Along the southernmost San Andreas fault, it has been argued that changes in the level of Lake Cahuilla, a remnant of which is the Salton Sea, might have changed the rate of seismicity for large earthquakes (Luttrell et al., 2007; Brothers et al., 2011; Philibosian et al., 2011). However, the lack of an accurate lake-level chronology together with an overview of earthquake activity in the Salton Trough impeded further progress.

The Salton Trough is host to the North America-Pacific plate boundary distributed principally among three major fault zones: the San Andreas, San Jacinto and Elsinore faults. Much of the slip from these faults becomes concentrated southward along the Imperial fault, which transfers slip across the international border to the Cerro Prieto fault, the northernmost transform fault extending out of the Gulf of California (Fig. 1). The earthquake records of virtually all fault strands of this plate boundary have been studied to some degree over the past 40 yrs. However, only a few studies in the Salton Trough (Gurrola and Rockwell, 1996; Rockwell et al., 2000a, 2011; Philibosian et al., 2011; Castillo et al., 2021) have developed earthquake records that extend back ~1200 yrs, either because sedimentation was very high, resulting in very deep exposures, or because the sediment record was incomplete. Prior to about 900 CE, lake chronology indicates an extended dry period in the Salton Basin (Gurrola and Rockwell, 1996; Rockwell et al., 2000a, 2022a) with the previous lakes dating to about 0-600 BCE (Lake G of Rockwell et al., 2022a) and older.

* Corresponding author.
E-mail address: trockwell@sdsu.edu (T.K. Rockwell).

https://doi.org/10.1016/j.epsl.2023.118271

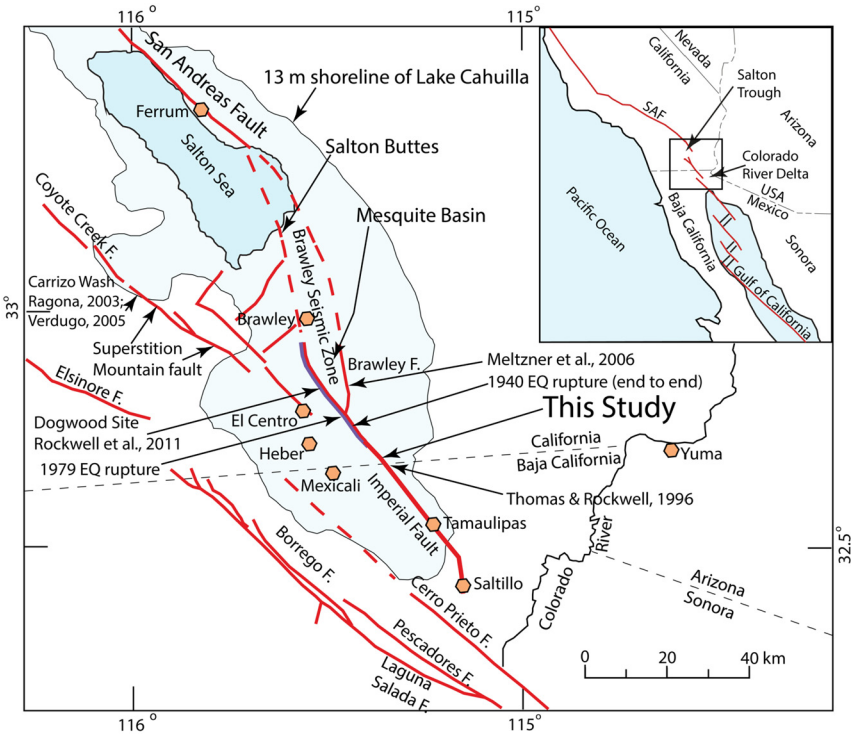

Fig. 1. Map of the southern Salton Trough region showing the extent of prehistoric Lake Cahuilla, the present-day Salton Sea, major faults, selected prior study sites along the Imperial fault, and this study area. Orange hexagons are larger towns. The 1979 rupture is indicated in blue along the northern third of the fault, whereas the 1940 earthquake ruptured end-to-end.

The timing of the late Holocene high-stands of Lake Cahuilla is well-dated and shows that there were six complete fillings of the basin between about 900 and ca 1730 CE (Rockwell et al., 2022a). The lake inundated sections of several major faults, including the San Andreas, San Jacinto, Imperial, and Cerro Prieto faults (Fig. 1). The lake inundations not only provide excellent stratigraphy at the many paleoseismic sites around the basin, but also allow for a coeval stratigraphic framework from which to correlate the paleoevents documented at the various sites. However, because of the depositional hiatus prior to about 900 CE, a longer view of the possible relationship between lake inundations and earthquakes has remained elusive as there were no paleoseismic results that extended into the dry period to assess the rate of earthquake production.

To recover a long paleoseismic records along the southern San Andreas Fault system in the Salton Trough is difficult. The high sedimentation rate results in young stratigraphic sections that are too thick to be trenched by conventional methods. Here, we apply Cone Penetrometer Testing (CPT) technology (Grant et al., 1997) to the International Border paleoseismic site (Jerrett, 2015; Wessel, 2015) along the Imperial fault, which is part of the main southern San Andreas fault system (Fig. 1). This site is located well into the inundation area of Lake Cahuilla, which has filled six times in the past 1100 yrs, and several more times earlier in the Holocene (Rockwell et al., 2022a). The chosen site corresponds to a small extensional basin which subsided during the large 1940 M∼7 Imperial Valley earthquake; the basin had no geomorphic expression prior to the earthquake (see Fig. S1 in the supplementary material) (Rockwell and Klinger, 2013). CPT is an ideal tool for subsurface studies because clayey lake deposits are easily distinguished from silty sand deltaic sediments. Unlike typical paleoseismological trenches, CPT allows for stratigraphic exploration for several tens of meters downward. Long records are important to test earthquake recurrence models. In the case of the southernmost San Andreas fault system, in fact it allows exploring the effects of lake loading on the occurrence and frequency of large earthquakes, and in particular, why the current open interval on the San Andreas fault is twice as long as the average earthquake recurrence interval (Philibosian et al., 2011).

The ratio of subsidence and lateral displacement at this sag is discretely known for the 1940 M7 Imperial Valley earthquake (Rockwell and Klinger, 2013; Jerrett, 2015; Wessel, 2015) as the topographic surface slope is very low (less than a meter per kilometer). Hence, apparent vertical offset must be due to vertical motion rather than lateral offset of dipping strata. If the ratio remains reasonably similar from earthquake to earthquake, we can also use the discrete subsidence per event information to infer variations in slip rate for the past 2 ka. There are many examples of repeating vertical displacements of similar magnitude or development of accommodation space at releasing steps activated during large earthquakes (Klinger et al., 2003; Rockwell et al., 2009, 2015). Hecker et al. (2013) compiled paleoseismic displacement data from 171 sites in 20 countries that show that slip per event at a point has a coefficient of variation (CoV) of 0.5, arguing for similar displacement from event to event which supports the characteristic slip model. For the Imperial fault, the fault ruptured end to end in the M7 1940 earthquake, but experienced smaller displacement along the northern third of the fault, which re-ruptured in the M6.6 1979 earthquake. This led Sieh (1996) to infer a slip patch model in which sections of faults express similar displacement from event to event. Based on these observations, we infer that for similar end-to-end ruptures along the Imperial fault that produce large displacement at our study site, the lateral and vertical displacements likely have been relatively similar. Assuming no significant change in fault geometry from event to event, this implies that large displacements as in 1940 should produce similar amounts of subsidence from event to event such that we can infer short term variations in slip rate from variations in subsidence rate. Moreover, identification of discrete subsidence events is a direct proxy for the occurrence of large earthquakes.

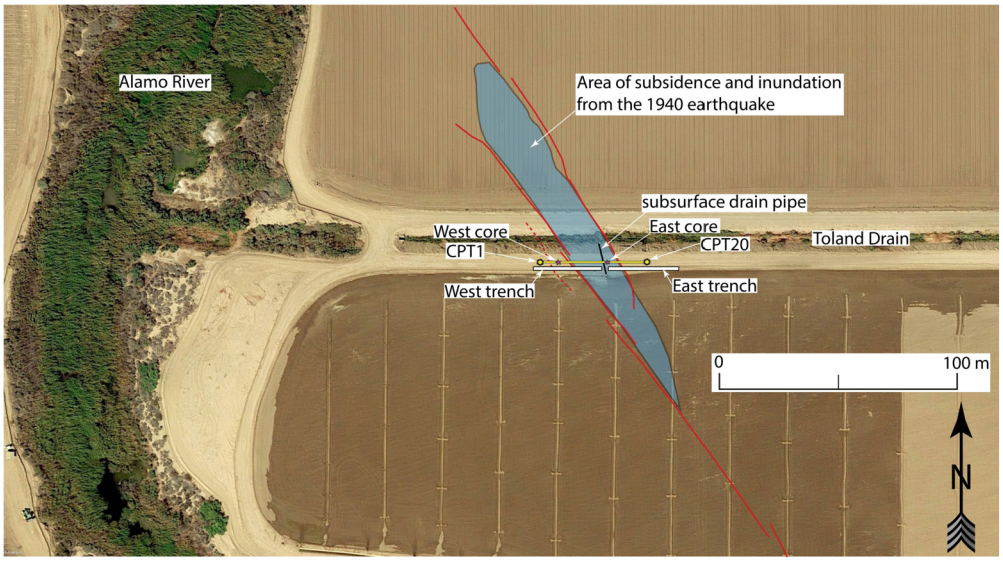

Fig. 2. Detailed map of the locations of the two trenches, CPT transect, and core locations between Gunterman Rd and the Alamo River along the south side of Toland Drain, located 0.8 km south of Highway 98. A subsurface pipe drains the southern field into Toland Drain, which required that the trenches be excavated in two sections. This also precluded pushing CPTs close to the subsurface pipe, resulting in the wide spacing between CPTs 11 and 13. Fault mapping is transferred from the detailed map of the 1940 rupture in Rockwell and Klinger (2013). Trench observations are detailed in Jerrett (2015) and Wessel (2015).

The study site is co-located with previous paleoseismic trenches that were excavated across a 20 m-wide releasing step (Fig. 2), producing a sag depression in the 1940 earthquake (Wessel, 2015; Jerrett, 2015; Rockwell and Klinger, 2013). In that preliminary work, the penultimate event occurred in Lake A and produced a similar amount of subsidence (∼1 m) as in 1940. Another two events, interpreted as smaller northern Imperial fault events because they are recognized in the lake strata in similar stratigraphic positions at the Dogwood site (Rockwell et al., 2011) produced a cumulative subsidence of about 6 cm. Notably, there was no evidence for these smaller events only 2 km to the southeast near the border (Thomas and Rockwell, 1996). Thus, the two small events are interpreted to represent 1979-type ruptures that involved displacement of the northern Imperial fault but produced little to no substantial slip at the border, whereas the 1940 and penultimate earthquake at ca 1730 (Rockwell et al., 2018, 2022a) each produced about 1 m of subsidence (Wessel, 2015; Jerrett, 2015). However, the 4-m-deep trench exposed sediments from only the three most recent lake inundations, and the sediments from the third lake (Lake C of Rockwell et al., 2018 and 2022a) were exposed only outside the sag as they had been dropped to below the base of the trench within the sag. Consequently, the trenching recorded only a 300–500 yr record of paleo-earthquakes, similar to that of Thomas and Rockwell (1996).

2. Methods

To lengthen the record, we emplaced CPT soundings at 1-4 m intervals across the entire width of the sag, extending to several meters beyond the margins of the depression to also capture the far-field deformation (Fig. 2). The CPTs were emplaced in three campaigns, with the first to explore the subsurface stratigraphy and the second and third to fill in details that were not captured in the first round. The CPT alignment was placed alongside and about 2 m to the north of the northern edge of the two trenches studied by Jerrett (2015) and Wessel (2015) (Fig. 2). We also drilled two continuous cores to directly observe the sediments, and to recover samples for radiocarbon dating.

The CPT cone records the resistance of being inserted into the ground (tip resistance) as well as the resistance to sliding through the sediment (sleeve friction) (Grant et al., 1997). The probe is mounted on a 25-ton truck that allows for deep penetration; the probe is inserted vertically into the ground and continuously records both tip resistance and sleeve friction as a function of depth. Hence, CPT soundings are ideal for identifying correlative strata in well-bedded stratigraphic sections. Fig. 3 shows the interpreted correlation of lacustrine (clayey silt and clay) and deltaic (silty sand and fine sand) sediments across the sag. The locations of the trenches are indicated in Figs. 2 and 3, as are the two cores with one core within and one outside the sag. In Fig. 3, the tip resistance and sleeve friction are plotted back-to-back and are extracted directly from the reporting sheets (PDFs) in Adobe Illustrator; the primary CPT reporting sheets from Middle Earth Geo Testing, Inc. are included in the supplementary material.

The locations of the radiocarbon samples are shown in Fig. 3, and the dates are presented in Table 1. Shell-bearing layers were extracted from the core in the Quaternary Laboratory at SDSU and rinsed in de-ionized water to separate shells, ostracods and charcoal from the sediment. These three components were separated under a microscope to concentrate each type of datable material. The two samples of charcoal were single detrital chunks, and each was dated separately. The ostracods are tiny and samples that contained at least several dozen shells were combined as a single sample and dated. Similarly, the shells were of the gastropod species *Tryonia protea*, which average a few mg each in mass. We selected 5 lustrous shells from each sample to combine for a single date. Samples were taken to the CAMS facility at UC Irvine and processed for AMS ^{14}C dating. The charcoal was treated with acid-base-acid (1N HCl and 1N NaOH at 75 degree C) prior to combustion. Shell and ostracod samples were leached 50% with dilute HCl prior to hydrolysis with 85% phosphoric acid. The ^{14}C dates were converted to calendar years in OxCal v. 4.4 (Bronk-Ramsey, 2021) using the marine 13 curve (Reimer et al., 2020) with a delta R correction of 0±20 for Lake Cahuilla (Rockwell et al., 2022b).

Using the regional lake-stratigraphic sequence, which is informed by nearly 300 radiocarbon dates on lake and inter-lake periods from several paleoseismic sites and a study of drowned stumps within the Lake Cahuilla basin (Gurrola and Rockwell, 1996; Philibosian et al., 2011; Rockwell et al., 2011, 2018), complemented by additional dating from our cores, we correlate the succession of clayey strata recognized by CPT and core to the well-dated lake sequence (Rockwell et al., 2018, 2022a). Specifically, we

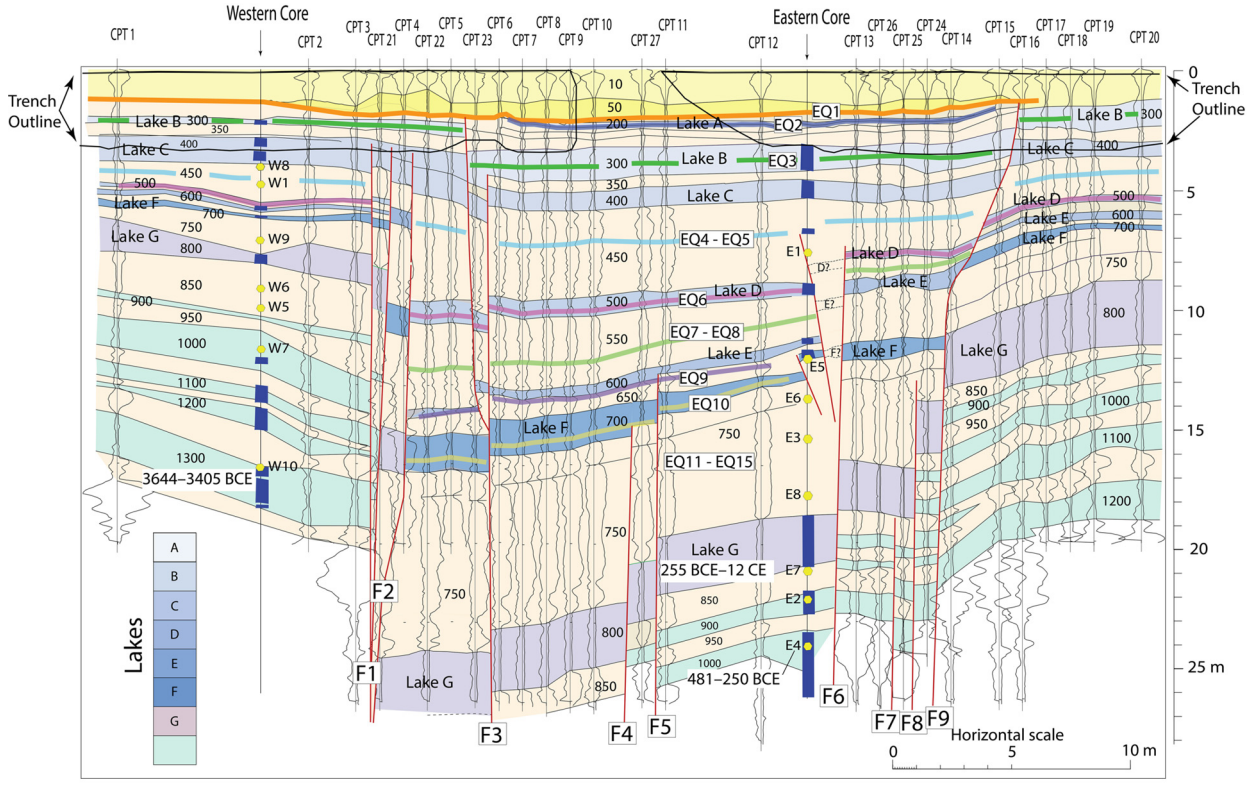

Fig. 3. CPT soundings and interpretation of correlative strata across the sag depression that was reactivated in the 1940 Imperial Valley earthquake. Note the distinctive CPT signature for unit 800, correlated to Lake G of Rockwell et al. (2022a). Also note the outlines of trenches excavated at the site in which the upper stratigraphy and faulting was exposed (Jerrett, 2015; Wessel, 2015). Notably, some lacustrine clay layers appear thinner in the cores than interpreted from the CPT data, possible due to the siltier sediment liquefying during the core recovery process. The locations of continuous cores are shown, along with the locations of ^{14}C samples recovered from the cores; the dark blue boxes along the cores are where lacustrine clay was noted in the core. The horizontal and vertical scales are equal. The CPT units are shown in Fig. 4 and the supplementary material but cannot be displayed here due to the scale. The tip resistance is the right side of each CPT, whereas the sleeve friction is mirrored (flipped over) on the left of each CPT (see explanation in Fig. 4). The interpreted earthquake horizons (EQ) are based on abrupt increases in subsidence, with some supported by the apparent terminations of some fault strands and are shown as colored contacts. Note that some event horizons are only shown in the sag because the section is compressed on the west and including thickened contacts obscures the CPT signature. The small events from the trench study are not included. ^{14}C ages for dates that exhibit little to no age inheritance are shown near their sample location; all ^{14}C locations are indicated by yellow hexagons.

tied unit 800 to Lake G of Rockwell et al. (2022a) based on radiocarbon dating and on the thick non-lacustrine section of unit 750 which is consistent with a long period of no lakes (but occasional delta flooding events). Unit 850, which represents deltaic sedimentation prior to the clay deposition of unit 800 and is interpreted to represent the filling phase of lake G, yielded a radiocarbon date that matches the age of Lake G. Underlying strata interpreted from two older lakes are consistent with this interpretation. The late Holocene lake sequence was then correlated based on the presence of lacustrine versus delta deposits, and from direct correlation in the previous trench investigations.

3. Results

The lacustrine (clayey) strata produced a signature with very low tip resistance whereas the silty sand strata exhibited higher tip resistance. Sleeve friction was variable but slightly higher in the deltaic sediments. The interpretation of delta vs lacustrine was confirmed using the continuous cores, as well as the previous exposures in the trenches (Jerrett, 2015; Wessel, 2015). However, we experienced some issues with the cores during extraction as the silty sand deltaic sediments tended to liquefy for some of the core recovery, which apparently thinned some of the clayey silt layers associated with the lake clays. Hence, the clearly-lacustrine clay layers in the core tended to be thinner than inferred from the CPT data, which are not disrupted by the coring process.

The units follow the numbering scheme initiated in the trenches (Jerrett, 2015; Wessel, 2015), with artificial fill near the surface as unit 10 with unit numbers increasing downward. Unit 200 corresponds to Lake A (ca 1731-1733 CE), unit 300 corresponds to Lake B (ca 1618-1636 CE), and unit 400 corresponds to Lake D (ca 1486-1503) (Rockwell et al., 2022a). The numbering scheme from the trenches used numbers in the hundreds to correspond to interpreted lakes and numbers between successive hundreds to correspond to deltaic sediments, and we extend that scheme here. Notably, much of the deltaic sequence likely represents the inundation or filling phase of the lake deposits that immediately overlie it, although it is possible that some deltaic sedimentation simply occurred during minor flooding events. Unit 800 is interpreted to correspond to Lake G of Rockwell et al. (2022a) based on radiocarbon dating.

The CPT signatures for each sounding are distinctive and along with the continuous cores, allow for correlation of stratigraphic units across the sag depression (Fig. 3). As CPT spacing ranged from 1 to 4 m (most are spaced at 1 m), the normal ambiguities of applying CPT data for subsurface evaluation were almost non-existent as the CPT signature for individual stratums as well as packages of strata were largely unique. However, the main faults on the western side of the graben express much of the vertical displacement and pose some issues with correlation of units across or within this fault zone. Our primary focus is on the strata from Lake G and above, so we compared the CPT signature of the upper part of the section across the fault to confirm the correlations of strata (Fig. 4). The sedimentation rate on the east side of the fault was slightly higher after deposition of Lake G strata, possibly due to a small east-side-down component of displacement (although juxta-

Table 1
Radiocarbon dates on shell (sh), ostracods (ostr), and detrital charcoal (ch) from the eastern and western cores shown in Fig. 3. The high-lighted dates are the only ones that follow stratigraphic ordering and were used to constrain the lake ages and correlate Lake G to the regional lake model of Rockwell et al. (2022a). The other dates exhibit significant age inheritance from reworking of older shells and ostracods, with the charcoal dates being the worst (presumably because of the abundant old wood in the Colorado Plateau region). Sample W8 is not highlighted because it is older than dates from the paleoseismic trenches from the same unit (Jerrett, 2015; Wessel, 2015) and exhibits some age inheritance.

UCIAMS #	Sample name	Depth (m)	Unit	fraction Modern	±	$D^{14}C$ (‰)	±	^{14}C age (BP)	±	Calibrated age range
210454	W8 -Sh	3.7	450	0.8125	0.0016	-187.5	1.6	1670	20	650-811 CE
210440	W1 - Ostr	4.6	450	0.8325	0.0016	-167.5	1.6	1475	20	818-1027 CE
210453	W1 - Sh	4.6	450	0.7586	0.0014	-241.4	1.4	2220	15	35-242 CE
210433	E1- Ostr.	7.5	450	0.8064	0.0014	-193.6	1.4	1730	15	586-721 CE
214821	E1 sh @ 8m redo	7.5	450	0.8061	0.0015	-193.9	1.5	1730	15	614-750 CE
210446	E1 - Sh	7.5	450	0.7843	0.0014	-215.7	1.4	1950	15	352-561 CE
210451	E5 – Sh	12	650	0.6616	0.0012	-338.4	1.2	3320	15	1351-1089 BCE
210462	E5- Char	12	650	0.2290	0.0007	-771.0	0.7	11840	30	11799-11620 BCE
214823	E5-Sh	12	650	0.6134	0.0011	-386.6	1.1	3925	15	2069-1855 BCE
210439	W9 - Sh	7.0	750	0.6882	0.0012	-311.8	1.2	3000	15	912-766 BCE
210452	E6 – Sh	13.7	750	0.6072	0.0011	-392.8	1.1	4010	15	2193-1956 BCE
210436	E6 – Ost	13.7	750	0.6159	0.0055	-384.1	5.5	3890	80	1929-1680 BCE
210448	E3 – Sh	15.4	750	0.6191	0.0011	-380.9	1.1	3850	15	1965-1746 BCE
210449	E3 –Sh	15.4	750	0.6160	0.0010	-384.0	1.0	3890	15	2016-1801 BCE
210434	E3 – Ostr	15.4	750	0.6266	0.0012	-373.4	1.2	3755	15	1846-1616 BCE
214822	E3 Shell	15.4	750	0.6100	0.0014	-390.0	1.4	3970	20	2128-1902 BCE
214825	E8 @ 58	17.7	750	0.7025	0.0013	-297.5	1.3	2835	15	772-512 BCE
210438	W6 - Sh	9.0	850	0.5889	0.0011	-411.1	1.1	4255	20	2539-2286 BCE
210437	W5 - Sh	9.8	850	0.5430	0.0012	-457.0	1.2	4905	20	3376-3101 BCE
210463	W5 -Char	9.8	850	0.3898	0.0010	-610.2	1.0	7565	25	6461-6401 BCE
214824	E7 Sh @	20.9	850	0.7384	0.0016	-261.6	1.6	2435	20	255 BCE -12 CE
210447	E2 – Sh	22	900	0.6887	0.0012	-311.3	1.2	2995	15	881-754 BCE
210435	E4 - Ostr	24	1000	0.6892	0.0014	-310.8	1.4	2990	20	855-732 BCE
210450	E4 - Sh	24	1000	0.7197	0.0012	-280.3	1.2	2640	15	481-250 BCE
210455	W10 - Sh	16.4	1300	0.5277	0.0011	-472.3	1.1	5135	20	3644-3405 BCE
214874	W7 Roots	11.6		0.9743	0.0016	-25.7	1.6	210	15	1651-1950 CE

position of slightly different thicknesses of units could also explain this as the fault has moved upwards of 60 m laterally since deposition of this unit). Fig. 4 shows the correlation of strata across the fault with the upper part of the section (Lake G and younger strata) slightly compressed on the northeast side; Lake G is the first lacustrine section encountered below deltaic sediments associated with the approximately 1 ka dry period between lakes G and F (Rockwell et al., 2022a). We are confident in correlation of strata above unit 900 in Fig. 3, and less certain for the older lakes.

The radiocarbon dating demonstrates a profound amount of reworking of gastropod and ostracod shells based on the large number of dates that violate stratigraphic ordering. As each shell date represents a sample composed of 5 individual *Tryonia protea* shells, the resulting age is the average age of the individual shells. Similarly, the ostracod shell samples were composed of dozens of individual shells. Although we tried to pick out only pristine and lustrous gastropods for dating, the only other plausible explanation other than profound reworking is that the some of the shells and ostracods were derived from far up the Colorado River where there may have been abundant dead carbon in the water that skewed the ages to the old side. This is not the likely explanation at Ferrum, where Rockwell et al. (2022b) show that about 90% of *Tryonia protea* shells are reworked, with ages ranging from about 550 yrs to over 7000 yrs. The youngest shell dates at Ferrum calibrate to Lake A at ca 1730 applying a delta R correction of zero (which we used in our analysis). Reworking appears to be a significant issue with shells in the Lake Cahuilla basin, which is not surprising considering that there are numerous lacustrine gastropods scattered across the desert floor below the shoreline; these will undoubtedly be remobilized should the basin ever be allowed to fill again. Based on the above, we use the youngest dates from any given stratigraphic unit as maximum ages for that stratum, and we assume that all dates that are older from overlying units exhibit some degree of either reworking or dead carbon age inheritance. Applying this logic, sample E7 from unit 850 either is older than or dates the filling of Lake G (unit 800) at 255 BCE to 12 CE, consistent with the age of Lake G at 612 to 5 BCE (Rockwell et al., 2022a). Similarly, sample E4 (sh) from unit 1000 yielded a slightly older age of 481 to 250 BCE, stratigraphically consistent with sample E7, and sample W10 from unit 1300 yielded an age of about 5.5 ka (Table 1). In contrast, all samples from units 650 to 850 yielded ages that ranged between about 500 and 6400 BCE (2.5-8.4 ka) older than the ages from units 850 and 1000. Consequently, we infer that 80-90% of the dates have some degree of age inheritance, similar to what was determined at Ferrum (Rockwell et al., 2022b). From the limited number of valid radiocarbon dates along with the sequence of stratigraphy, units 500, 600, and 700 in Fig. 3 are interpreted to correlate to Lakes D, E, and F in Rockwell et al. (2022a).

One important aspect to note is that most sedimentation occurs when the Colorado River avulses north from its normal flow to the Gulf of California (Sea of Cortez) and flows down the Alamo and New Rivers to fill, partially or completely, the Lake Cahuilla basin. Complete filling of the basin requires only 12-20 yrs, depending on the flow rate of the Colorado River (Rockwell et al., 2018). Between such flows, there is probably little to no deposition on this area of the Colorado delta, implying that much of the section studied here resulted from fairly short periods of deltaic flooding of the basin (silty sand deposits) followed by deeper water lacustrine deposition of the clayey strata if the flow resulted in a full lake. Once the river avulses back to its channel towards the Gulf, deposition in the basin effectively stops, resulting in a period of non-deposition. As there have been several historical flows into the basin that did not result in full lakes, including from 1905 to 1907 which resulted in the formation of the Salton Sea (Cory, 1915), it is probable that some sedimentation may have occurred in the vicinity of the CPT line between lakes, especially considering its proximity to the Alamo River, but we do not see evidence of coarser fluvial channel alluvium above about 17 m depth: CPT1, which is closest to the Alamo River, exhibits a distinct coarsening at this depth which could be evidence that the channel was closer

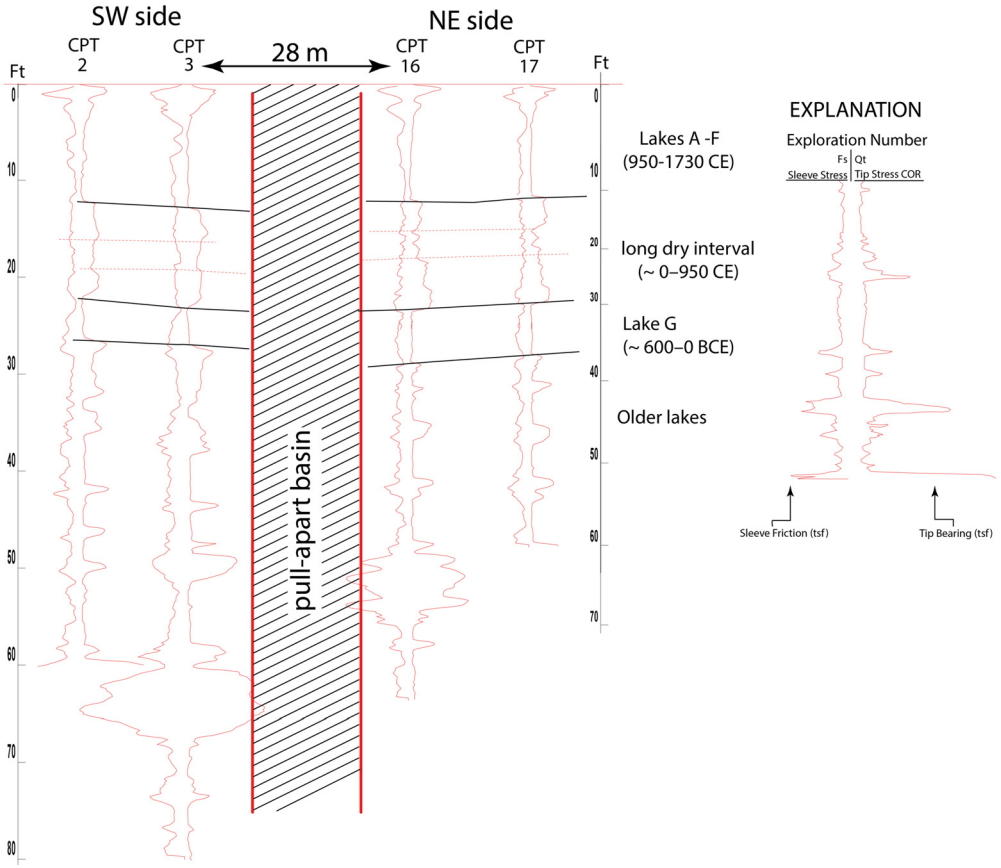

Fig. 4. Comparison of CPTs 2 and 3 southwest of the fault with CPTs 16 and 17 northeast of the pull-apart basin. Note that the depositional environments of these CPTs were not only separated by nearly 30 m but also by however much displacement has occurred on the fault since deposition of individual strata, as much as 60 m. The sedimentation rate was apparently a somewhat higher northeast of the fault since the time of Lake G so the section is slightly thicker relative to the southwest side. Nevertheless, the only reasonable correlation is to match the first long lacustrine episode after the long delta phase, as shown. Older lakes below Lake G (unit 800) also match reasonably well, at least in the upper part of the section. The scale on the right shows the amount of compression of the section needed for the best match. The scale is in feet, as that is how the data were collected by the CPT rig.

to the fault during deposition of strata older than unit 1300. For these flows, it seems reasonable that a sag depression would fill quickly if accommodation space was available.

Based on the interpreted correlations of strata in Fig. 3, we measured the amount of subsidence for each lake stratum (Table 2) (Measurements are presented in Figs. S29 to S34 in the supplemental material). The thick clayey section associated with Unit 800 is well-correlated through the entire CPT line and provides a basis for interpreting the lacustrine deposits associated with units 500, 600 and 700 (interpreted to correlate to lakes F, E, and D). Sediments from lakes C, B, and A were exposed in the trenches in the upper 3.5 m of the profile and correlate well to units 400, 300 and 200, respectively.

To quantify subsidence, we compared the elevations of the tops and bottoms of the interpreted lake strata within the sag and at their highest points at the far ends of the CPT lines, CPT1 and CPT20 (presented as Figs. S29 through S34 in the supplementary material). The rational for this is that there is clear warping and minor faulting affecting the stratigraphy adjacent to the bounding faults which accommodate some of the vertical signal. In contrast, the surface geomorphology demonstrates that the natural slope is on the order of a meter per kilometer. Consequently, we infer that the apparent vertical warping is tectonic and should be included in the analysis of vertical displacement. Notably, the vertical displacements measured in the trenches (Jerrett, 2015; Wessel, 2015) likely underestimate the actual full vertical displacement because they only account for slip on the bounding faults in the trench exposures and not the far-field warping or slip from minor fault strands.

Large earthquakes are interpreted where there is an abrupt increase in vertical separation across the bounding fault strands (Table 2). We also identified structural evidence for discrete ruptures where lower strata are displaced by faults and then possibly capped by unbroken strata within the step-over, although these are not the basis of the interpretations in Table 2. Notably, many of these secondary faults predate the stratigraphy exposed in the trenches where no evidence of faulting was observed above the locations of the buried faults.

Based on measurements as described above and presented in Table 2, the sag has experienced ~18.5 m of subsidence in the past ~2.1 ka relative to the SW side of the fault, and 15.5 m relative to the NE side of the fault since deposition of the top of unit 800, indicating a long-term NE-side down sense of separation (Fig. 3). The top (T) and bottom (B) estimates of subsidence relative to the eastern and western sides of the fault are presented in Table 2 for each interpreted lake unit. The amount of subsidence within or between lake units is estimated when there is an abrupt increase in subsidence between successive contacts (VD column in Table 2). For instance, the base of unit 500 has subsided about 6.05 m relative to the western block and about 5.35 m relative to the eastern block, whereas the top of unit 600 has subsided about 9.2 m and 8.4 m relative to the western and eastern blocks, respectively. This indicates that an additional 3 to 3.2 m of subsidence occurred between deposition of units 500 and 600. This subsidence could have occurred any time between these lacustrine deposits during a delta

Table 2
Measurements of vertical separation (VD) on lake strata for the eastern and western sides of the sag depression based on the trench observations (near-field measurements in parentheses for units 50, 200 and 300: Jerrett, 2015; Wessel, 2015) and correlation and interpretation of CPT soundings (far-field measurements). Each lake deposit was measured at the top and bottom (T / B) of the interpreted stratum, as presented in the supplemental material. Measurement uncertainty for the far-field separation is about 10-20 cm. Note that the near-field trench measurements are minimums. Also note that the base of unit 800 (Lake G) was not penetrated by the CPT so the vertical estimate is a minimum value. The small events are those described in Jerrett (2015) and Wessel (2015) and exhibit a total of 6 cm of vertical separation and subsidence in the sag.

Unit	Lake	T / B	West Side (m)	East Side (m)	VD (m)	Event
50	—	T	—	(0.93)	(0.93)	EQ1 (1940)
200	A	T	—	(1.8)	(0.87)	EQ2 (~1730)
200		B	(1.0)	(1.86)		
300	B	T	1.45 (0.95)	2.15 (1.86)	(<0.1)	small events
300		B	2.4	2.4 (1.8)	0.35-0.95	EQ3 (~1628)
400	C	T	2.5	2.3		
400		B	2.4	2.6		
					2.45-2.75	EQ4, EQ5 (?)
500	D	T	5.2	4.9		
500		B	6.05	5.35	0.45-0.85	EQ6
					3-3.2	EQ7, EQ8 (?)
600	E	T	9.2	8.4		
600		B	9.3	8.3		
					~0.5	EQ9
700	F	T	9.8	8.9		
700		B	11.1	10.2	1.3	EQ10
					5.3-7.4	EQ11, EQ12 EQ13, EQ14 (EQ15?)
800	G	T	18.5	15.5		
800		B	19.4	15.9	0.4-0.9	Q15? or EQ16

Approx. ages of units: Unit 200 (Lake A) – 1731-1733 CE, Unit 300 (Lake B) – 1618-1636 CE, Unit 400 (Lake C) – 1486-1503 CE, Unit 500 (Lake D) – 1192-1241 CE, Unit 600 (Lake E) – 1007-1070 CE, Unit 700 (Lake F) – 930-966 CE, and Unit 800 (Lake G) – 612-5 BCE (Rockwell et al., 2022a).

depositional phase or at the end of deposition of lacustrine unit 600 or the beginning of lacustrine unit 500. In contrast, the base of unit 700 is offset more than the top, which suggests the occurrence of a subsidence event during deposition of the lacustrine section itself.

Analysis of the amount of subsidence for each stratigraphic unit indicates the occurrence of six 0.5-1.3 m subsidence events and a couple of 2.5-3 m subsidence events in the past 1100 yrs. We interpret each of these larger subsidence events to represent two earthquakes with 1.25-1.5 m subsidence per earthquake. It is possible that the large subsidence events result from single earthquakes, but that would require 2 to 3 times the amount of subsidence than that which occurred in conjunction with 6 m of lateral slip in 1940, which we consider unlikely as that implies either very large lateral slips or that the amount of subsidence is coincidentally a factor of two larger than the average smaller subsidence events. Determination of the exact amount of subsidence for each singular earthquake, however, is hindered by our limited resolution in the spacing of the tops and bottoms of lacustrine contacts. If multiple earthquakes occurred during the period of lake infill dominated by deltaic sedimentation, rather than during a full-lake period undergoing clayey deposition, it is not possible to resolve the discrete subsidence associated with each of them. Another issue is that if an event occurred during the filling phase during deltaic sedimentation, it will appear to be associated with a dry period. In this model, some of the subsidence associated with a "double" event may have actually occurred as the lake was nearly full, in which case that event would have actually been associate with a lake highstand. Accordingly, we interpret that there have been as many as 15-16 earthquakes in the past 2.3±0.3 ka, including the four or five events that we interpret to be associated with the 5.3-7.4 m of vertical offset that accrued between lakes G and F and an event in Lake G itself.

The rate of subsidence was relatively slow at about 5.5-7.1 mm/yr between about ~2.3 and 1.1 ka ago, as estimated from the slope of the lines in Fig. 5 for subsidence relative to the western and eastern sides of the fault, respectively. This is a period during which no lakes are known to have filled the basin (Rockwell et al., 2011, 2022a). Subsidence accelerated to about 17 mm/yr after inundation by Lake F (unit 700) at about 950 CE, and this higher rate persisted for about 300-400 yrs during the period of lakes F, E, and D (units 700, 600, and 500) before slowing down to about 5.1-5.4 mm/yr, a rate similar to that which preceded Lake F (Fig. 5).

4. Discussion

The CPT observations document 15.5-18.5 m of subsidence (top unit 800) that occurred as discrete events in the past ~2.1 ka, of which 10 large events occurred in the past 1.1 ka and probably several more between 1.1 and 2.1 ka. The observation that ~1 m of subsidence in 1940 was produced when 6 m of lateral slip passed through the sag suggests that previous ~1 m subsidence events, such as in ca 1730, may have resulted from earthquakes similar to 1940, in which the entire Imperial fault ruptured end-to-end. Altogether, six subsidence events since ca 950 CE, including the 1940 earthquake, produced larger or smaller amounts of subsidence, and the average vertical displacement for these six events is a little over 0.8 m, which is close to that observed for 1940 and 1730 (although the 1940 and 1730 events probably have low estimates as they were only measured in the near-field). We

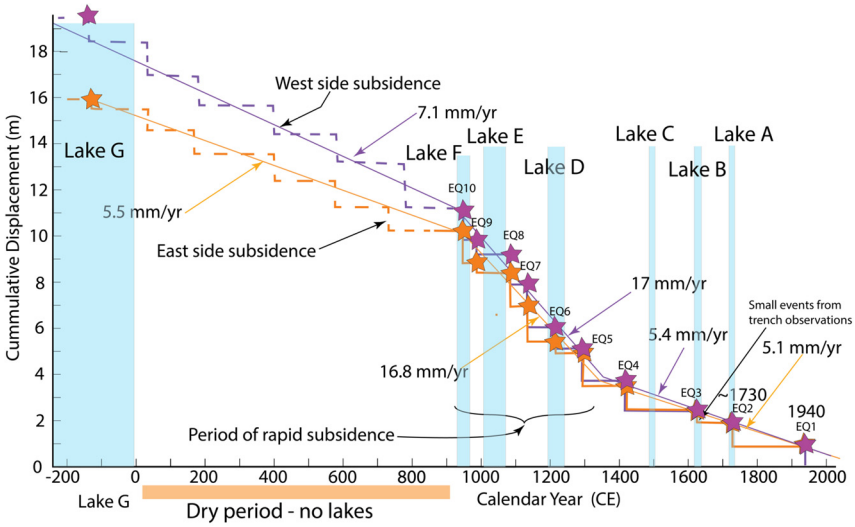

Fig. 5. Plot of subsidence through time for the past 2.2 ka, with interpretation of earthquakes (stars) as inferred from the historical record and trench results (EQ1, EQ2, minor events documented in Jerrett, 2015 and Wessel, 2015), abrupt large subsidence events and faults capped by undeformed strata inferred from the CPT transect data. The inferred subsidence per event is indicated by the bold lines, whereas the subsidence rate is indicated by the finer sloping lines. The periods of lake highstand are indicated by the vertical blue bands (from Rockwell et al., 2022a).

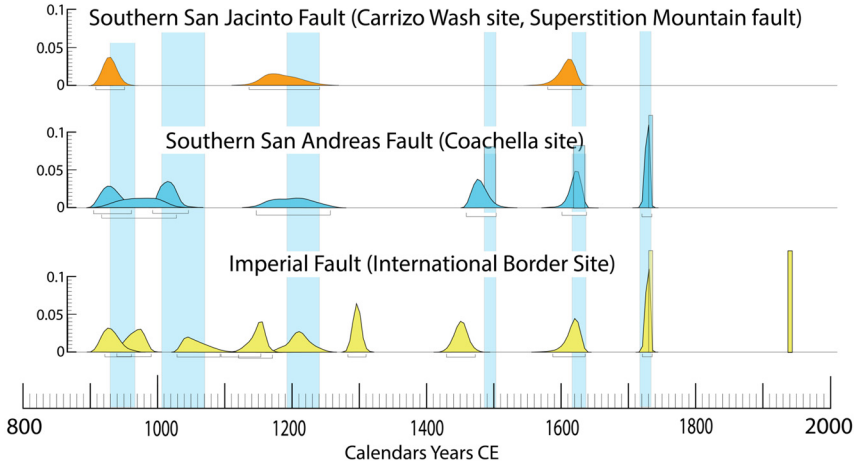

Fig. 6. Probability distributions generated by OxCal based on placing the event horizons into the regional model for Lake Cahuilla (Rockwell et al., 2022a). The lightly-shaded boxes are distributions trimmed by the historical record and a climate model. The brackets below the PDFs represent the 95% confidence intervals.

interpret all of these to be large earthquakes that produced significant lateral slip across the international border, although the ~half-meter subsidence events may represent somewhat smaller slips.

Two other interpreted events produced ~2.5-3.2 m of subsidence, which is a factor of two or more larger than the 1940-type events. If there is any relationship between subsidence and lateral slip, it is difficult to envision that the Imperial fault produced lateral displacements events that are twice as large as the 1940 earthquake, especially considering the relatively high heat flow (Sibson, 1982) and relatively shallow seismic locking depth (Smith-Konter et al., 2011). We consider it more likely that these double-sized subsidence events represent two earthquakes so we interpret them as such. Thus, we interpret that there were 10 large subsidence events in the past 1100 yrs yielding an average subsidence per event of 1 to 1.1 m relative to the eastern and western sides of the fault, respectively.

Six or seven of these earthquakes occurred in the 300-400 yrs after inundation by Lake F whereas only three or four occurred in the following 600-700 yrs up to the present day. This represents a substantially higher rate of subsidence, and hence, interpreted earthquake occurrence, in the period after Lake F filled the basin, and this was followed by a period of less subsidence and therefore fewer interpreted earthquakes (Fig. 5).

The only other two paleoseismic records that extend back to and include Lake F are the Coachella paleoseismic site on the San Andreas fault (Philibosian et al., 2011) and the Carrizo Wash site on the Superstition Mountain strand of the southern San Jacinto fault (Rockwell et al., 2000a; Ragona et al., 2001; Ragona, 2003; Verdugo, 2005). The stratigraphic context of some sedimentary units at the Coachella site was reinterpreted by Rockwell et al. (2022a) because some lacustrine deposits had been misclassified as non-lacustrine. Specifically, the presence of organic mats, which are only found around the basin below the shoreline of ancient Lake Cahuilla, was reinterpreted to represent organic accumulations from inundations by the lake rather than soils in this hyper-arid environment. Consequently, the evidence for events Coa3 (weak) and Coa4 (strong) was combined as they both are now interpreted to have occurred during the inundation phase of Lake C. Similarly, the "persistent" organic layer associated with unit S5 at Coachella was reinterpreted by Rockwell et al. (2022a) to represent the inundation phase for Lake D. In addition, event Coa8 occurred in deposits that are reinterpreted to date to the time of Lake F, so that event is included in this analysis. We recalcu-

lated the earthquake ages at the Coachella site (Fig. 6) using the new lake model of Rockwell et al. (2022a), including the reinterpreted stratigraphy as presented in the electronic supplement to Rockwell et al. (2022a), and using the stratigraphic position of the earthquake event horizons, as presented in Philibosian et al. (2011) (The Oxcal model for Coachella is presented in the Supplementary Material). Six of the seven events are now interpreted to have occurred during lake phases, and four of the seven events occurred during the first 300-350 yrs after inundation by Lake F, with the other three in the ensuing 750-800 yrs (Fig. 6).

Similarly, we recalculate the ages of the three large slip events at the Carrizo Wash site on the southern San Jacinto fault, all of which experienced about 2 m of lateral displacement (Ragona, 2003), using the lake model of Rockwell et al. (2022a) (The Oxcal model is presented in the Supplementary Material). For Carrizo Wash, the stratigraphy is described in the electronic supplement to Rockwell et al. (2022a), and the earthquake interpretations are unchanged from Ragona (2003) and Verdugo (2005). Two events occurred in the first 300-350 yrs after inundation of Lake F whereas only one event has occurred in the past 750-800 yrs (Fig. 6).

The above observations demonstrate that the frequency of earthquakes on the southernmost San Andreas, San Jacinto and Imperial faults all shows a similar pattern with more earthquakes during the few hundred yrs after inundation by Lake F, and fewer earthquakes in the ensuing 750-800 yrs after lake D. Only the longer record on the Imperial fault demonstrates that the more frequent earthquake activity during lakes F through D follows a period of fewer earthquakes during the long dry period between lakes G and F. Nevertheless, the observed pattern argues for a basin-wide signal that requires a system-level explanation.

Luttrell et al. (2007) interpreted the increase in weight due to lake loading as the primary mechanism to decrease the strength of the San Andreas fault, as the lake center is off to the west of the fault. However, the Imperial fault lies within the basin and should be unaffected by weight as both sides are equally loaded. Hence, we interpret the above observations as primarily a signal of transient variations in pore pressure at seismogenic depth (Healy et al., 1968; Raleigh et al., 1976; Ellsworth, 2013; Keranen et al., 2014; Keranen and Weingarten, 2018). The dry period would result in a decrease in pore pressure and an increase in fault strength, and a consequent additional accumulation in elastic strain. New modeling by Hill et al. (2023) directly modeled the effect of pore pressure variations and conclude that fluctuations in lake level likely modulated earthquakes on the San Andreas fault.

We suggest that this effect was basin-wide. When the basin was once again filled with water to 13 m elevation during Lake F, resulting in ~100 m of water depth, an increase in pore pressure, and a decrease in fault strength, these faults are interpreted to have released the extra accumulated elastic strain by producing more frequent earthquakes. This would also result in increased slip rates on these faults in the first few hundred years after inundation. This latter idea is explored further below, but our new data on the Imperial fault supports this assertion if the amount of lateral slip is in any way related to the amount of subsidence per event in the sag pond that we explored.

Once the system re-equilibrated to the new conditions, crustal loading, which in the far-field would not be expected to change, continued to load the fault and produce earthquakes at a rate that is similar to the dry period before Lake F. This is indicated by the subsidence rate at the Imperial sag which exhibits a rate for the past 750-800 yrs that is very similar to the rate between Lakes G and F between 2.1–2.4 ka and 1.1 ka. As all three studied faults exhibited the same post Lake F behavior (Fig. 6), we infer that this basin-wide effect may have affected all faults within the Salton Trough.

4.1. Slip rate considerations on the Imperial fault

The slip rate on the Imperial fault, the primary fault in the San Andreas fault system crossing the US-Mexico border, is estimated to range from 20 mm/yr to 36 mm/yr (Thomas and Rockwell, 1996; Bennett et al., 1996; Meade and Hager, 2005; Smith-Konter et al., 2011; Lindsey and Fialko, 2016). Part of this uncertainty reflects the time span and the methods used to resolve rate. Most of these rates are based on geodetic models that assumed that the Imperial fault was the only major strand crossing the international border. The Thomas and Rockwell (1996) rate was based on a very short geologic record of less than 500 yrs, and may therefore be biased by too short of an observation period. Resolution of slip per event for the past 2,000 yrs of earthquakes for a site on the Dead Sea fault shows that the slip rate can vary over several earthquake cycles and that at least 8-10 events are required to average out the long-term slip rate (Wechsler et al., 2018). The southern San Andreas fault system may require an even longer time period to reach a meaningful average slip-rate considering the issue of fluctuating lake levels.

If our assumption that the amount of subsidence per event is at least roughly correlated to lateral slip, then this suggests that slip rate also accelerated after about 900 CE when Lake F filled the basin after the extended dry spell. Using the 5.5 m of average slip that occurred in the border region in the 1940 earthquake (Rockwell and Klinger, 2013), and assuming that each large subsidence event results from similar lateral slip, at least on average, the ten events that occurred since about 900 CE would have produced about 55 m of lateral displacement (although two of the subsidence events were smaller at about 0.5 and 0.65 m, so this may be a slight exaggeration), which is nearly equal to the plate rate. Between about 900 and 1300 CE, we document the occurrence of five or six events, which would imply 27.5 to 33 m of lateral slip in only ~400 yrs, resulting in a much higher rate of ~70 to 80 mm/yr, much higher than the plate rate. In contrast, the past ~700 yrs have only experienced three or four such large earthquakes, yielding a much lower rate of 23 to 32 mm/yr, which is in the middle of current rate estimates.

Assessing the rate between 2.3±0.3 ka and 1.1 ka is more difficult using this method because we do not know the precise number of large events. However, there was ~5-7 m of subsidence within the pond, and using the average subsidence per event (1-1.1 m) suggests the occurrence of five to seven earthquakes in this time interval. That would equate to ~27.5 to 37.5 m of lateral slip in ~ 1.2 ka, yielding a slip rate for this period of ~23 to 31 mm/yr, which is similar to the current rate suggested by Lindsey and Fialko (2016). Considering the entire 2.3±0.2 ka period, and applying the 10 events since 1.1 ka and the additional 5 to 7 events between 2.3±0.2 and 1.1 ka, 13-15 such slip events would yield a slip rate of 34 to 39 mm/yr using the 5.5 m average slip per event, consistent with the higher estimates of the current rate (Bennett et al., 1996; Meade and Hager, 2005).

The overall observation is that the subsidence rate, and therefore the inferred slip rate, was lower when water was absent from the basin and then accelerated greatly when the basin was once again filled with water. This observation stands regardless of the number of earthquakes interpreted or inferred between lakes G and F. These data argue strongly that the presence or absence of 100 m of water in the Salton Trough affects the strength of the Imperial fault. The Imperial fault is loaded equally in terms of weight so the likely major mechanism is the increase in pore pressure which reduces the effective normal stress (Hill et al., 2023), although the increase in water weight adjacent to the San Andreas fault may also be a factor for that fault (Luttrell et al., 2007). Brothers et al. (2011) also argue that lake loading triggers large southern San Andreas fault earthquakes, and it has now been nearly 300 yrs

since the last large surface rupture (Rockwell et al., 2018). However, they did not develop a specific chronology to see the effects of lake loading on the frequency of earthquakes so our study is the first to directly show the relationship between the rate of earthquake production and lake loading.

One consequence of the effects of pore pressure is that it has now been 300 yrs since the last complete filling of Lake Cahuilla and the fault may now be stronger as a result. This may explain the apparent "earthquake drought" on the southern San Andreas fault, as it has been 300 yrs since the last large earthquake. Alternatively, the recurrence interval on all three faults presented in this study had relatively short periods between large events for the several hundred years after inundation by Lake F, whereas the past 700 yrs or so have seen a longer recurrence interval by about a factor of two. Taken in perspective, the apparently longer open interval on the southern San Andreas fault may simply be more representative of the recurrence interval during dryer times rather than being "overdue" for an earthquake.

A last point, which is more speculative, is that the apparent increase in seismicity along the Imperial fault coincides with a period of more intense seismicity in southeastern California. The past thousand years have seen a cluster of large earthquakes in the Eastern California Shear Zone (Rockwell et al., 2000b), so there is the possibility that the change of seismicity rate due to the transient effect of lake loading may have a medium distance effect on the rate of earthquake production in nearby regions.

5. Conclusions

We show that the Imperial fault probably experienced a transient increase in slip rate that possibly exceeded the plate rate during the burst of seismic activity that followed the long dry period between Lakes G and F. We also have demonstrated that the southern San Andreas and Superstition Mountain faults in the Salton Trough experienced a higher rate of earthquake production in the several hundred-year period after inundation of Lake Cahuilla following the long dry interval than in the past 700-800 yrs. We attribute these variations in seismic activity to be related to variations in pore pressure that have directly affected the strength of the faults within the basin. As the region has apparently transitioned into another dry period for the past 300 yrs, the long open interval on the southern San Andreas fault may simply reflect the re-strengthening of the fault rather than the fault being "overdue" for an earthquake. This may also support the idea that the 3-4 m of slip along the southern San Andreas fault during the past few earthquakes (Blanton et al., 2020) may be exceeded in the next southern San Andreas rupture, with as much as 5-6 m of slip (Fialko, 2006).

CRediT authorship contribution statement

Thomas K. Rockwell: Conceptualization, Data curation, Formal analysis, Funding acquisition, Investigation, Methodology, Project administration, Writing – original draft, Writing – review & editing. **Yann Klinger:** Conceptualization, Formal analysis, Investigation, Writing – original draft, Writing – review & editing.

Declaration of competing interest

The authors have no competing interests.

Data availability

Data will be made available on request.

Acknowledgements

This work was supported by USGS Grant No. G18AP0004 to Rockwell and Klinger. We thank the Imperial Irrigation District for granting access to the site, and to D. Brothers and an anonymous reviewer for providing detailed comments and suggested changes that led to improvement in the presentation of this work.

Appendix A. Supplementary material

Supplementary material related to this article can be found online at https://doi.org/10.1016/j.epsl.2023.118271.

References

Bennett, R.A., Rodi, W., Reilinger, R.E., 1996. Global positioning system constraints on fault slip rates in southern California and northern Baja California, Mexico. J. Geophys. Res. 101 (B10), 21.

Bettinelli, P., Avouac, J.P., Flouzat, M., Bollinger, L., Ramillien, G., Rajaure, S., Sapkota, S., 2008. Seasonal variations of seismicity and geodetic strain in the Himalaya induced by surface hydrology. Earth Planet. Sci. Lett. 266 (3–4), 332–344.

Blanton, C.M., Rockwell, T.K., Gontz, A., Kelly, J., 2020. Refining the spatial and temporal signatures of creep and co-seismic slip along the southern San Andreas fault using very high resolution SfM imagery, Coachella valley, California. Geomorphology 357, 107064. https://doi.org/10.1016/j.geomorph.2020.107064.

Bronk-Ramsey, 2021. OxCal v. 4.4.4. https://c14.arch.ox.ac.uk/oxcal/.

Brothers, D., Kilb, D., Luttrell, K., Driscoll, N., 2011. Loading of the San Andreas fault by flood-induced rupture of faults beneath the Salton Sea. Nat. Geosci. 4, 486–492. https://doi.org/10.1038/NGEO1184.

Castillo, B.A., McGill, S.F., Scharer, K.M., Yule, D., McPhillips, D., McNeil, J., Saha, S., Brown, N.D., Moon, S., 2021. Prehistoric earthquakes on the Banning strand of the San Andreas fault, North Palm Springs, California. Geosphere 17 (3), 685–710. https://doi.org/10.1130/GES02237.1.

Cory, H.T., 1915. The Imperial Valley and the Salton Sink. John J. Newbegin, San Francisco, California.

Ellsworth, W.L., 2013. Injection-induced earthquakes. Science 341 (6142). https://doi.org/10.1126/science.1225942.

Fialko, Y., 2006. Interseismic strain accumulation and the earthquake potential on the southern San Andreas fault system. Nature 441 (22). https://doi.org/10.1038/nature04797.

Freed, A.M., Ali, S.T., Burgmann, R., 2007. Evolution of stress in southern California for the past 200 years from coseismic, postseismic and interseismic stress changes. Geophys. J. Int. 169, 1164–1179.

Grant, L.B., Waggoner, J.T., Rockwell, T.K., von Stein, C., 1997. Paleoseismicity of the north branch of the Newport-Inglewood fault in Huntington beach, California. Bull. Seismol. Soc. Am. 87, 277–293.

Gurrola, L.D., Rockwell, T.K., 1996. Timing and slip for prehistoric earthquakes on the superstition mountain fault, Imperial valley, southern California. J. Geophys. Res. 101, 5977–5985. https://doi.org/10.1029/95JB03061.

Healy, J.H., Rubey, W.W., Griggs, D.T., Raleigh, C.B., 1968. The Denver earthquakes. Science 161 (3848), 1301–1310.

Hecker, S., Abrahamson, N.A., Wooddell, K.E., 2013. Variability of displacement at a point: implications for earthquake-size distribution and rupture hazard on faults. Bull. Seismol. Soc. Am. 103 (2A), 651–674. https://doi.org/10.1785/0120120159.

Hill, R., Weingarten, M., Fialko, Y., Rockwell, T., 2023. Major earthquakes on the southern San Andreas fault modulated by lake filling events. Nature, 1–6. https://doi.org/10.1038/s41586-023-06058-9. First published online.

Jerrett, A., 2015. Paleoseismology of the Imperial fault at the US-Mexico border and correlation of regional lake stratigraphy through analysis of oxygen/carbon isotope data. Unpublished MS thesis. San Diego State University.

Keranen, K.M., Weingarten, M., 2018. Induced seismicity. Annu. Rev. Earth Planet. Sci. 46 (1), 149–174.

Keranen, K.M., Weingarten, M., Abers, G.A., Bekins, B.A., Ge, S., 2014. Sharp increase in central Oklahoma seismicity since 2008 induced by massive wastewater injection. Science 345 (6195), 448–451.

King, G.C.P., Stein, R.S., Lin, J., 1994. Static stress changes and the triggering of earthquakes. Bull. Seismol. Soc. Am. 4 (3), 935–953.

Klinger, Y., Sieh, K., Altunel, E., Akoglu, A., Barka, A., Dawson, T., Gonzalez, T., Meltzner, A., Rockwell, T., 2003. Paleoseismic evidence of characteristic slip on the western segment of the North Anatolian fault, Turkey. Bull. Seismol. Soc. Am. 93 (6), 2317–2332.

Lefevre, M., Klinger, Y., Al-Qaryouti, M., Le Béon, M., Moumani, K., 2018. Slip deficit and temporal clustering along the Dead Sea fault from paleoseismological investigations. Sci. Rep. 8 (1), 4511.

Lindsey, E.O., Fialko, Y., 2016. Geodetic constraints on frictional properties and earthquake hazard in the Imperial valley, southern California. J. Geophys. Res., Solid Earth 121, 1097–1113. https://doi.org/10.1002/2015JB012516.

Luttrell, K., Sandwell, D.T., Smith-Konter, B., Bills, B., Bock, Y., 2007. Modulation of the earthquake cycle at the southern San Andreas fault by lake loading. J. Geophys. Res. 112 (B8), B08411. https://doi.org/10.1029/2006JB004752.

Meade, B.J., Hager, B.H., 2005. Block models of crustal motion in southern California constrained by GPS measurements. J. Geophys. Res. 110, B03403. https://doi.org/10.1029/2004JB003209.

Philibosian, B., Fumal, T., Weldon, R., 2011. San Andreas fault earthquake chronology and lake Cahuilla history at Coachella, California. Bull. Seismol. Soc. Am. 101, 13–38. https://doi.org/10.1785/0120100050.

Ragona, D., 2003. A high-resolution paleoseismic study in the southern San Jacinto fault zone, Imperial County, California. M.S. thesis. San Diego State University.

Ragona, D., Rockwell, T.K., Orgil, A., 2001. Fault segmentation and earthquake behavior: a high resolution paleoseismic study in the southern San Jacinto fault zone. In: AGU Fall Meeting Abstracts, vol. 2001, S52D-0668.

Raleigh, C.B., Healy, J.H., Bredehoeft, J.D., 1976. An experiment in earthquake control at Rangely, Colorado. Science 191 (4233), 1230–1237.

Reimer, P., Austin, W., Bard, E., Bayliss, A., Blackwell, P., Bronk Ramsey, C., Butzin, M., Cheng, H., Edwards, R., Friedrich, M., Grootes, P., Guilderson, T., Hajdas, I., Heaton, T., Hogg, A., Hughen, K., Kromer, B., Manning, S., Muscheler, R., Palmer, J., Pearson, C., van der Plicht, J., Reimer, R., Richards, D., Scott, E., Southon, J., Turney, C., Wacker, L., Adolphi, F., Büntgen, U., Capano, M., Fahrni, S., Fogtmann-Schulz, A., Friedrich, R., Köhler, P., Kudsk, S., Miyake, F., Olsen, J., Reinig, F., Sakamoto, M., Sookdeo, A., Talamo, S., 2020. The IntCal20 Northern Hemisphere radiocarbon age calibration curve (0-55 cal kBP). Radiocarbon 62, 725–757. https://doi.org/10.1017/RDC.2020.41.

Rockwell, T.K., Dewhurst, J.A., Walls, C.W., Pollard, W.J., Orgil, A., Faneros, G., Dawson, T.E., 2000a. High-resolution paleoseismology in southern California: investigation of segment controls on the rupture history of the southern San Jacinto fault: in active fault research for the New Millenium. In: Okumura, K., Takada, K., Goto, H. (Eds.), Proceedings of the Hokudan International Symposium and School on Active Faulting. Letter Press Ltd., Hiroshima, Japan, pp. 413–419.

Rockwell, T.K., Lindvall, S., Herzberg, M., Murbach, D., Dawson, T., Berger, G., 2000b. Paleoseismology of the Johnson valley, Kickapoo and Homestead valley faults of the eastern California shear zone. Bull. Seismol. Soc. Am. 90 (5), 1200–1236.

Rockwell, T., Ragona, D., Seitz, G., Langridge, R., Barka, A., Aksoy, E., Ucarkus, G., Akbalik, B., Satir, D., Meltzner, A., Klinger, Y., Meghraoui, M., Ferry, M., 2009. Paleoseismology of the North Anatolian fault near the Marmara sea: implications for fault segmentation and seismic hazard. In: Reicherter, K., Michetti, A.M., Silva, P.G. (Eds.), Paleoseismology: Historical and Prehistorical Records of Earthquake Ground Effects for Seismic Hazard Assessment. In: The Geological Society of London Special Publications, vol. 316, pp. 31–54.

Rockwell, T.K., Dawson, T.E., Young-Ben Horton, J., Seitz, G., 2015. A 21 event, 4,000-year history of surface ruptures in the anza seismic gap, San Jacinto fault and implications for long-term earthquake production on a major plate boundary fault. Pure Appl. Geophys. 172 (5), 1143–1165. https://doi.org/10.1007/s00024-014-0955-z.

Rockwell, T.K., Klinger, Y., 2013. Surface rupture and slip distribution of the 1940 Imperial valley earthquake, Imperial fault, southern California: implications for rupture segmentation and dynamics. Bull. Seismol. Soc. Am. 103 (2A), 629–640. https://doi.org/10.1785/0120120192.

Rockwell, T.K., Meltzner, A., Tsang, R., 2011. A long record of Earth- quakes with timing and displacements for the Imperial fault: a test of earthquake recurrence models. Final Technical Report, U.S. Geological Survey Grant No. G10AP00003. 28 pp.

Rockwell, T.K., Meltzner, A., Haaker, E., 2018. Dates of the two most recent surface ruptures on the southernmost San Andreas fault recalculated by precise dating of Lake Cahuilla sediments. Bull. Seismol. Soc. Am. 108 (5A), 2634–2649. https://doi.org/10.1785/0120170392.

Rockwell, T.K., Meltzner, A.J., Haaker, E., Madugo, D., 2022a. The late Holocene history of lake Cahuilla: two thousand years of repeated fillings within the Salton Trough, Imperial valley, California. Quat. Sci. Rev. 282, 107456. https://doi.org/10.1016/j.quascirev.2022.107456.

Rockwell, T., Buckley, W., Williams, P., Gontz, A., 2022b. Testing Recurrence Models for the southernmost San Andreas Fault by Developing a New Paleoseismic Site at Durmid, Salton Trough: Collaborative Research with SDSU and USGS. Final Technical Report for USGS NEHRP Award No. G21AP10005. 46 pp.

Scharer, K., Streig, A., 2019. The San Andreas fault system: complexities along a major transform fault system and relation to earthquake hazards. In: Transform Plate Boundaries and Fracture Zones. Elsevier, pp. 249–269.

Smith-Konter, B.R., Sandwell, D.T., Shearer, P., 2011. Locking depths estimated from geodesy and seismology along the San Andreas fault system: implications for seismic moment release. J. Geophys. Res., Solid Earth 116, B06401. https://doi.org/10.1029/2010JB008117.

Sibson, R., 1982. Fault zone models, heat flow, and the depth distribution of earthquakes in the continental crust of the United States. Bull. Seismol. Soc. Am. 72 (1), 151–163.

Sieh, K., 1996. The repetition of large earthquake ruptures. Proc. Natl. Acad. Sci. 93, 3764–3771.

Stein, R.S., Barka, A.A., Dieterich, J.H., 1997. Progressive failure on the North Anatolian faulty since 1939 by earthquake stress triggering. Geophys. J. Int. 128, 594–604.

Thomas, A.P., Rockwell, T.K., 1996. A 300-550 year history of slip on the imperial fault near the U.S.-Mexico border: missing slip at the imperial fault bottleneck. J. Geophys. Res. 101 (B3), 5987–5997.

Verdugo, D., 2005. Further resolution of past earthquake surface ruptures at Carrizo Wash, southern San Jacinto Fault, Imperial Valley, California: the devil is in the deposits. Unpublished seniot thesis. San Diego State University. 18 pp.

Wechsler, N., Rockwell, T.K., Klinger, Y., 2018. Variable slip-rate and slip-per-event on a plate boundary fault: the Dead Sea fault in northern Israel. Tectonophysics 722, 210–226. https://doi.org/10.1016/j.tecto.2017.10.017.

Wessel, K., 2015. 500 year rupture history of the Imperial fault at the international border through analysis of faulted Lake Cahuilla sediments, carbon-14 data, and climate data. Unpublished MS thesis. San Diego State University.